JACS
JOURNAL OF THE AMERICAN CHEMICAL SOCIETY

Article

Selective Methane Oxidation to Methanol on Cu-oxo Dimers Stabilized by Zirconia Nodes of NU-1000 Metal–Organic Framework

Jian Zheng, Jingyun Ye, Manuel A Ortuño, John L. Fulton, Oliver Y. Gutiérrez, Donald M. Camaioni, Radha Kishan Motkuri, Zhanyong Li, Thomas E. Webber, B. Layla Mehdi, Nigel D. Browning, R. Lee Penn, Omar K. Farha, Joseph T. Hupp, Donald Truhlar, Christopher J. Cramer, and Johannes A. Lercher

J. Am. Chem. Soc., **Just Accepted Manuscript** • Publication Date (Web): 22 May 2019

is published by the American Chemical Society. 1155 Sixteenth Street N.W., Washington, DC 20036

Selective Methane Oxidation to Methanol on Cu-oxo Dimers Stabilized by Zirconia Nodes of NU-1000 Metal–Organic Framework

Jian Zheng,[†⊗] Jingyun Ye,[‡⊗] Manuel A. Ortuño,[‡] John L. Fulton,[†] Oliver Y. Gutiérrez,[†] Donald M. Camaioni,[†] Radha Kishan Motkuri,[#] Zhanyong Li,[⊥] Thomas E. Webber,[§] B. Layla Mehdi,[θ] Nigel D. Browning,[θ] R. Lee Penn,[§] Omar K. Farha,[⊥∥] Joseph T. Hupp,[⊥] Donald Truhlar,[‡] Christopher J. Cramer,[‡] and Johannes A. Lercher*[†Δ]

[†]Institute for Integrated Catalysis, and Fundamental and Computational Science Directorate, Pacific Northwest National Laboratory Richland, Washington 99354, USA
[‡] Department of Chemistry, Supercomputing Institute, and Chemical Theory Center, University of Minnesota, Minneapolis, Minnesota 55455, USA
[#] Energy and Environment Directorate, Pacific Northwest National Laboratory, Richland, Washington 99354, USA
[⊥] Department of Chemistry, Northwestern University, Evanston, Illinois 60208, USA
[§] Department of Chemistry, University of Minnesota, Minneapolis, Minnesota 55455-0431, USA
[θ] School of Engineering, University of Liverpool, Liverpool, L69 3GH, United Kingdom
[∥] Department of Chemistry, Faculty of Science, King Abdulaziz University, Jeddah 21589, Saudi Arabia
[Δ] Department of Chemistry and Catalysis Research Institute, TU München, Lichtenbergstrasse 4, 85748 Garching, Germany

KEYWORDS: Methane oxidation, methanol production, metal-organic framework, ion-exchange, Cu XAFS.

ABSTRACT: Mononuclear and dinuclear copper species were synthesized at the nodes of NU-1000 metal–organic framework (MOF) via cation exchange and subsequent oxidation at 200 °C in oxygen. Copper-exchanged MOFs are active for selectively converting methane to methanol at 150–200 °C. At 150 °C and 1 bar methane, approximately a third of the copper centers are involved in converting methane to methanol. Methanol productivity increased by 3-4 fold and selectivity increased from 70 % to 90 % by increasing the methane pressure from 1 to 40 bar. Density functional theory showed that reaction pathways on various copper sites are able to convert methane to methanol, the copper oxyl sites with by far lower free energy barriers. Combining studies of the stoichiometric activity with characterization by *in situ* X-ray absorption spectroscopy and density functional theory, we conclude that dehydrated dinuclear copper oxyl sites formed after activation at 200° C are responsible for the activity.

INTRODUCTION

Direct conversion of methane to easily condensable oxygenated energy carriers under mild condition is conceptually a key reaction in the decentralized conversion of shale gas.[1-2] Enzymes such as particulate methane monooxygenase (pMMO) are able to convert methane to methanol at ambient temperature via active Cu sites.[3] Bioinspired catalysts, for example, tricopper complexes immobilized into mesoporous silica have shown activity for selective methane oxidation.[4-5] Similarly, copper- and iron-exchanged zeolites have attracted much attention recently due to their high methanol selectivity.[6-11] With these materials, methanol was produced by sequential dosing of oxygen and methane, followed by methanol extraction with the assistance of steam. Recently, Narsimhan et al. reported continuous catalytic pathway to convert methane to methanol on copper-exchange zeolites in a single pass.[12] However, despite these promising results, the low methanol yield caused by the low concentration of the active centers is still the main challenge to overcome.

Elucidating the structure of the active site to the selectivity of methanol is essential because methane activation poses strict structure requirements. In the case of copper exchanged zeolites, the dinuclear Cu species ($[Cu–O–Cu]^{2+}$) for ZSM-5 and mordenite (MOR) was first proposed as the active center.[13] Recently, trinuclear copper-oxo clusters in MOR[14] and ZSM-5[15] have been associated with high activity for methane partial oxidation. In contrast, a mono-copper $[CuOH]^{+}$ core in eight-membered ring (8MR) zeolites such as SSZ-13 has been suggested to an active site.[16] Bokhoven and co-workers have also shown that small dehydrated clusters with several Cu atoms in MOR are active, but only active at high methane pressure.[17]

Like zeolites, metal–organic frameworks (MOFs) have high porosity, and they have customizable pore environments via post-synthetic modification of linkers and nodes.[18-25] Moreover, most MOFs are crystalline solids with permanent ordered structures. This allows characterization by single-crystal and/or powder-diffraction techniques, and it facilitates the design of well-defined heterogeneous catalysts.[26-28] Two general types of active species stabilized by the MOFs have been proposed for activating the C-H bond of alkane. Namely, the own metal species of the MOF's building units and extra-framework metal sites formed via post-synthetic modifications

of the MOF.[29-33] For instance, the iron species in the structural position of Fe-MOF-74[27, 29] and Fe-MIL-53[34] have been shown active to convert alkanes to alcohols, although these sites may suffer from instability or low catalytic performance. Other examples are single-site cobalt and iron species formed via post-synthetic metalation at the nodes of zirconium- and hafnium-based MOFs that have been found active for C-H bond cleavage.[35-36] Recently, Baek et al. has shown that bis(μ-oxo) dicopper species incorporated into the pores of MOF, e.g. MOF-808, can selectively oxidize methane to methanol under mild conditions.[37]

NU-1000 is one of the most robust MOFs.[38] The terminal –OH groups on the zirconium oxide nodes of NU-1000 are ideal for chemical functionalization such as ion exchange or atomic layer deposition.[39-40] There are a number of examples highlighting the importance of dispersed metal atoms or clusters in NU-1000 for heterogeneous catalysis.[41-44] We have reported that atomic layer deposition of (ALD) copper clusters on the nodes of NU-1000 are selective for partial oxidation of methane to methanol. We concluded that a trimeric Cu-hydroxide-like structure bridging two nodes across the c-pore of NU-1000 is the active site.[45]

In order to probe a lower nuclearity of the Cu sites, we report the synthesis, characterization, kinetic exploration, and density functional theory (DFT) calculation of the catalytic activity towards oxidative functionalization of methane on monocopper and dicopper centers in NU-1000. The structural determination is based on a combination of spectroscopic and computational analysis. The structural changes of the copper species accompanying the reaction were probed via *in situ* X-ray adsorption spectroscopy (XAS). These findings are important for understanding the structure-activity relationships of metal exchanged MOFs for selective methane oxidation, and they provide new insights into the design of catalytic single atom and small clusters stabilized in the pores of MOFs.

RESULTS AND DISCUSSION

Preparation and characterization of copper exchanged Cu-NU-1000.

In this study, three Cu-NU-1000 samples were synthesized via aqueous phase cation exchange.[40] The loadings of Cu were 2.9 wt % (Cu-2.9-NU-1000, Cu/Zr_6 molar ratio = 1), 1.9 wt % (Cu-1.9-NU-1000, Cu/Zr_6 molar ratio = 0.65), and 0.6 wt % (Cu-0.6-NU-1000, Cu/Zr_6 molar ratio = 0.2). The synthesis and characterization of Cu-NU-1000 are detailed in the Experimental Section. It is worth noting that following the Cu exchange, we exchanged water with acetone as solvent before drying. This step is key to preserving the integrity of the framework, avoiding capillary-force-driven channel collapse due to the high surface tension of water (Figures S3 and S4).[46] Figure 1 shows characterizations of Cu-2.9-NU-1000. Similar results were obtained for the 0.6 and 1.9 wt % Cu-loaded samples. The XRD pattern shows that the crystal structure of Cu-2.9-NU-1000 is the same as that of pristine NU-1000 (Figure 1a). There are small decreases in the BET surface area (<10%), pore volume, and average size of the large pores, consistent with Cu being deposited into the large hexagonal channels of NU-1000 framework (Figure 1b and S30). Thermal gravimetric analysis (TGA) shows that the exchanged material is stable up to 300 ºC in air (Figure 1c). Transmission electron microscopy (TEM, Figure S6) and high-angle annular dark-field scanning transmission electron microscopy (HAADF-STEM, Figure 1d) images show that there are no observable Cu nanoparticles formed (> 1 nm). Elemental maps obtained by scanning transmission electron microscope–energy dispersive x-ray spectroscopy (STEM-EDS) show a homogeneous distribution of Cu throughout the MOF crystal (Figure 1e). Infrared spectroscopy shows that the spectral features are largely unchanged after Cu^{II} exchange (Figure S9a). However, the intensity decrease of the Zr-OH band at 3674 cm^{-1} indicates that Cu^{II} has exchanged protons of these -OH groups on the Zr_6 nodes (Figure S9b).[39] Taken together, these results show that the copper has been introduced into NU-1000 without altering the MOF framework structure.

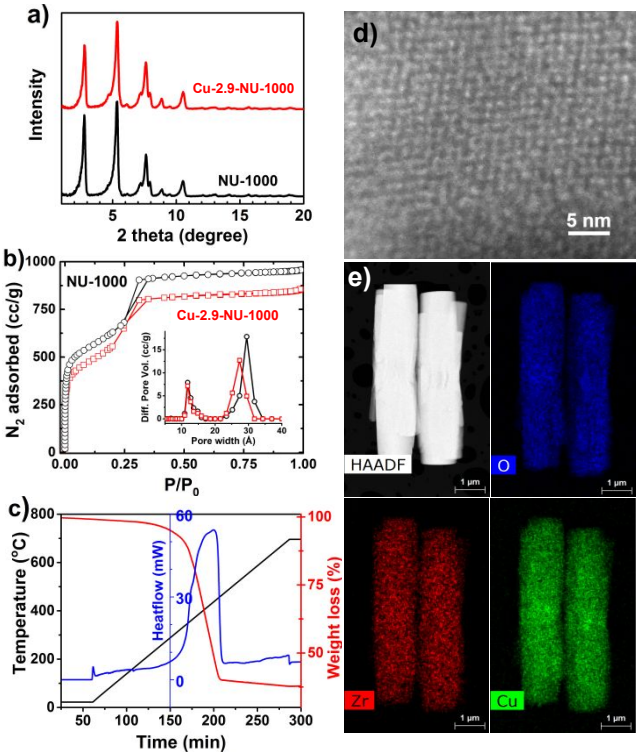

Figure 1. (a) XRD patterns and (b) N_2 adsorption and desorption isotherms measured at 77 K of Cu-2.9-NU-1000 compared with parent NU-1000; Insert of (b) shows pore size distributions; (c) TG graphs of Cu-2.9-NU-1000 measured for the sample in compressed air with temperature ramp of 3 K per minute from room temperature to 700 °C; (d) High-angle annular dark field (HAADF) image; and (e) STEM-EDS elemental maps of Cu-2.9-NU-1000.

Cu K-edge X-ray absorption near-edge structure (XANES) and extended X-ray absorption fine structure (EXAFS) were used to assess the local structure of Cu in NU-1000. Figure 2a shows the normalized XANES spectra for Cu-2.9-NU-1000, $Cu(OH)_2$, Cu_2O, CuO, and aqueous Cu^{II}. The XANES of Cu in NU-1000 is similar to that of the $Cu(OH)_2$ reference. The pre-edge feature at 8978 eV (inset) is assigned to the 1s → 3d transition of Cu^{II} species.[47] The intensity of this spectral feature is also close to that of $Cu(OH)_2$. A pre-edge shoulder

corresponding to Cu^{I} at 8983 eV was not observed.[48] The 0.6 and 1.9 wt. % Cu exchanged samples exhibited XANES spectra nearly identical to that in Figure 2a for the 2.9 wt. % sample (Figure S12 shows a comparison of the three Cu-exchanged NU-1000 samples).

Figure 2b shows the phase-uncorrected k^2-weighted $\chi(R)$ spectra for Cu-2.9-NU-1000 (black curve) and the reference compounds. The first feature centered at ~1.5 Å is assigned to the Cu-O single scattering. We observe that the first shell structure of Cu in the MOF is nearly identical to that of $Cu(OH)_2$, as they show the same bond distance and amplitude. The weak feature at ~2.0 Å is likely due to the elongated, Jahn–Teller (JT) out-of-plane distortion of O atom(s) that would be present in either the square pyramidal or the distorted JT-octahedral symmetries.[49-50] This feature is also observable in $Cu(OH)_2$, CuO, and aqueous Cu^{II}, but not in tetrahedrally coordinated Cu_2O.[51-52] We also note that the Cu-Cu single scattering feature (2.4 Å) in Cu-2.9-NU-1000 is weak compared to that of $Cu(OH)_2$, Cu_2O, and CuO references, and only slightly higher than that of isolated aqueous Cu^{II}, which has no Cu neighbors. This Cu-Cu coordination feature is especially weak in the samples (Cu-1.9-NU-1000 and Cu-0.6-NU-1000) having lower Cu loadings (Figure S13), and this suggest that Cu is present in very small entities, i.e., dimeric or trimeric Cu species possibly in a mixture with isolated Cu cations.

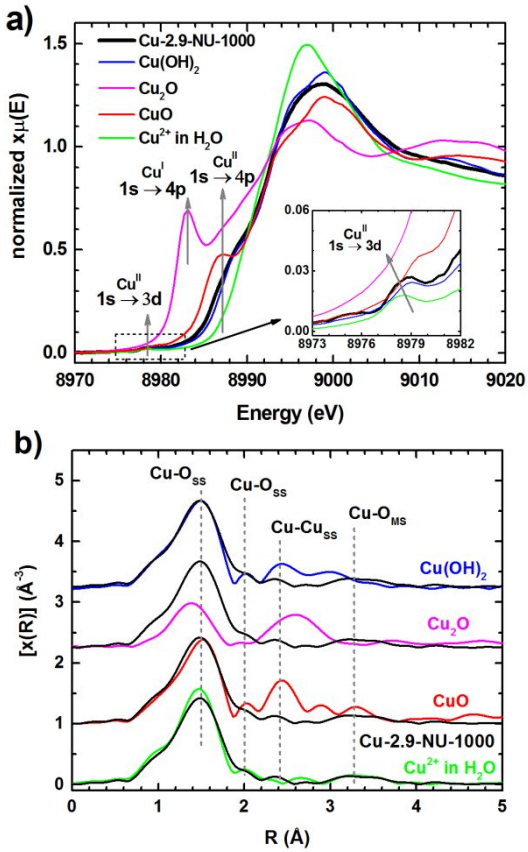

Figure 2. (a) Normalized Cu-XANES spectra and (b) k^2-weighted Cu-EXAFS $\chi(R)$ spectra of the as-prepared Cu-2.9-NU-1000 and reference compounds. The insert of a) shows the pre-edge feature at 8973–8982 eV corresponding to the 1s→3d electronic transition for the Cu^{II}. SS = single scattering, MS = multiple scattering.

Activity of Cu-NU-1000 for methane-to-methanol oxidation

Selective oxidation of methane was performed with Cu-NU-1000. We used three sequential reaction steps in a typical reaction cycle.[45] We firstly varied the methane loading time from 30 to 180 minutes to explore the impact of the methane contact time on methanol productivity on Cu-2.9-NU-1000. As shown in Figure 3a, the methanol yield increased from ~3.3 $mmol_{MeOH}/mol_{Cu}$ (1.5 $\mu mol_{MeOH}/g_{catalyst}$) (30 min) to 9.7 $mmol_{MeOH}/mol_{Cu}$ (4.4 $\mu mol_{MeOH}/g_{catalyst}$) (180 min). No obvious increase in methanol production was observed by further increasing the methane loading time. It suggests that the surface methane coverage was nearly saturated after 3 hours. Thus, activation with 1 bar oxygen at 200 °C and reaction with 1 bar methane at 150 °C yields the maximum amount of methanol formed per Cu of about 0.01. This efficiency observed here is comparable to that of ALD synthesized Cu-NU-1000,[45] but higher than that of Cu-MOR or Cu-ZSM after activation with oxygen or NO at 150–200 °C.[17, 53] It is also worth noting that the methanol selectivity of 70 % is higher than that of 40-60 % on previous ALD synthesized Cu-NU-1000.[45]

We also performed multiple catalytic cycles to show the stability and applicability of Cu-2.9-NU-1000 (Figure 3b). The methane loading time in the cycling test was fixed to 180 minutes. Methanol yield of about 9 $mmol_{MeOH}/mol_{Cu}$ was observed in each cycle, indicating only slight deactivation of the catalyst. The selectivity to methanol was stable over the five cycles at ~70%. Dimethyl ether (DME) was not observed. In order to confirm the methanol selectivity, we have used ^{13}C-methane as the reactant in the first step and performed the experiment under the same conditions. About 9 $mmol_{MeOH}/mol_{Cu}$ of ^{13}C-labelled methanol (m/z = 33) and ~4 $mmol_{CO2}/mol_{Cu}$ ^{13}C-labelled CO_2 (m/z = 45) were observed. Only minor amounts of $^{12}CO_2$ (m/z = 44, < 1 $mmol_{CO2}/mol_{Cu}$) were found. (Figure S17). Although some deactivation was observed in the first cycle, it is less significant in subsequent cycles. We attribute the initial deactivation to decarboxylation of free carboxylate groups.[45] This is consistent with the observation of trace amounts of CO_2 detected by the mass spectroscopy during the activation step in oxygen at 200 °C (Figure S16). These results demonstrate that Cu-NU-1000 is stable for this reaction.

Compared to 4.4 $\mu mol_{MeOH}/g_{catalyst}$ obtained from Cu-2.9-NU-1000, the methanol yields from Cu-1.9-NU-1000 and Cu-0.6-NU-1000 were lower at 2.3 and 0.45 $\mu mol_{MeOH}/g_{catalyst}$, respectively. A blank reaction under identical conditions using the pristine NU-1000 MOF lead to ~0.3 $\mu mol_{MeOH}/g_{catalyst}$, similar to our previous work reporting 0.4–0.5 $\mu mol_{MeOH}/g_{catalyst}$.[45] Assuming that the same amount of methanol is produced by the MOF itself from the Cu-exchanged NU-1000, the methanol productivities are 4.1, 2.0, and 0.15 $\mu mol_{MeOH}/g_{catalyst}$ for Cu-2.9-NU-1000, Cu-1.9-NU-

1000 and Cu-0.6-NU-1000 (Figure 3c, red bars). These are 9.7, 6.2 and 1.4 $mmol_{MeOH}/mol_{Cu}$ (Figure 3c, open bars) when normalized by the molar ratio of Cu. Thus, the methanol productivity per Cu atom of Cu-2.9-NU-1000 is 6.4-fold higher than that of Cu-0.6-NU-1000, although all samples exhibit the similar methanol selectivity of ~70% (inset in Figure 3c).

Increasing methane pressure enhances the coverage of activated species, which in turn enhances the extant of methane conversion and the selectivity to methanol in continuous operation.[54-56] An increased yield of methanol with increasing methane pressure was also recently observed for Cu-MOR zeolites.[7, 17] Thus, we further investigated the effect of methane pressure on methanol productivity with Cu-2.9-NU-1000. The catalyst was activated in 1 bar oxygen at 200 °C for 2 h. In the second step, methane at increasing pressure was contacted with the material at 150 °C or 200 °C. We observed an increase of the productivity of methanol correlated with the increase of methane pressure (Figure S18). Figure 3d shows a direct comparison of the catalytic performance of Cu-2.9-NU-1000 exposed to methane at 1 and 40 bar. The methanol productivity was 9.7 and 14.5 $mmol_{MeOH}/mol_{Cu}$ at 150 °C and 200 °C, respectively, at 1 bar. The productivity increased to 24.5 and 34.8 $mmol_{MeOH}/mol_{Cu}$ (150 °C and 200 °C) as methane pressure was increased to 40 bar. We also observed 1.4 and 2.0 $mmol_{DME}/mol_{Cu}$ of DME, which equals additional 2.8 and 4.0 $mmol_{MeOH}/mol_{Cu}$ of methanol. In contrast, changing the methane pressure has only negligible influence on the amounts of CO_2, which is 2.7 and 4.3 $mmol_{CO2}/mol_{Cu}$ at 150 °C and 200 °C at 40 bar. Taking these into account, the selectivity to methanol is ~90% at 40 bar at both temperatures. Thus, the maximum of methanol (including DME) productivity at 200 °C and 40 bar is 0.04 molecules per Cu atom. In terms of electron transfer, the formation of one molecule of methanol, dimethyl ether, and carbon dioxide requires 2, 4, and 8 electrons, respectively, transferred to copper (Cu^{II} reduced to Cu^{I}). Thus, there are 70 (35 mmol · 2), 8 (2 mmol · 4), and 34.4 (4.3 mmol · 8) mmol electrons involved in the formation of methanol, dimethyl ether, and carbon dioxide per each mol of copper. In a word, a total of 112.4 mmol Cu^{II} were reduced to Cu^{I} from each 1000 mmol copper to activate methane (11.2% of total Cu). To the best of our knowledge, this might be the highest value on the MOF-based catalysts for methane oxidation so far.

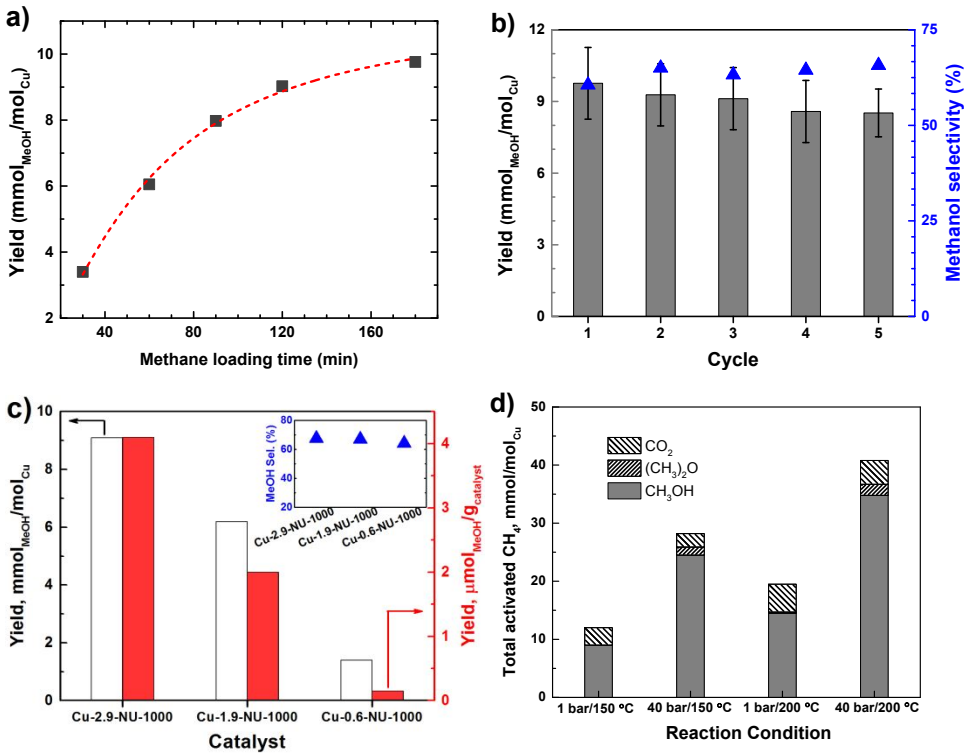

Figure 3. Catalytic testing of copper-exchanged NU-1000 for selective oxidation of methane to methanol: (a) Effect of methane loading time on methanol yield over Cu-2.9-NU-1000; (b) the activity over the first 5 catalytic cycles of Cu-2.9-NU-1000 and the selectivity to methanol; (c) catalytic activity comparison of the Cu exchanged NU-1000 samples; and (d) effect of temperature and methane pressure during the reaction. The catalyst was activated in 1 bar oxygen at 200 °C for 2 h, then 1 bar or 40 bar of methane was applied at 150 °C or 200 °C (30 to 180 minutes), and finally steam-assisted product was extracted with 10% H_2O and 90% He for 3 h at 135 °C. The products were analyzed on-line with a mass spectrometer.

Structure probing along the reaction

In situ XAS of Cu-2.9-NU-1000 was performed to probe structural variations in the active Cu sites along the reaction cycle. The sample was firstly heated in oxygen for 120

minutes at 200 °C. After cooling to 150 °C in O_2, the XANES spectrum was recorded *in situ* (Figure 4a, green curve). The XANES curve of this "O_2 activated" Cu-2.9-NU-1000 sample resembles the curve for the $Cu(OH)_2$ reference (Figure S14). There was a considerable decrease in the white line intensity after activation, similar to that observed during activation of Cu-zeolites.[57-58] This change is due to the removal of coordinating H_2O ligands, which are also supported by the EXAFS spectra that show (see as-synthesized and O_2-activated spectra in Figure 4b) a decrease in the amplitude of the first Cu-O single scattering (1.5 Å) and the disappearance of the second Cu-O scattering assigned to JT water (2.0 Å). Thus, we conclude that the out-of-plane water molecules are removed after heating in flowing O_2. Furthermore, the weak Cu-Cu single scattering feature at 2.4 Å demonstrates that the nuclearity of the Cu sites in NU-1000 is not changed by the heat treatment in oxygen.

As discussed above, the pre-edge XANES signal at 8977–8978 eV is assigned to the 1s→3d transition in Cu^{II}. Because Cu^{I} ion does not have this transition owing to the filled d^{10} orbital, this feature can be used as a fingerprint for the presence of Cu^{II}.[59] We note this feature is enhanced (insets of both XANES and first derivative XANES in Figure 4a) after activation, suggesting an increased interaction of Cu^{II} ion with the MOF framework due to the heat treatment, similar to that of Cu-exchanged zeolites.[60] We also note a loss of the intensity of the multiple scattering feature at ~3.3 Å, which suggests that the square planar structure of Cu is somewhat distorted by the thermal activation. Interestingly, there is an increase in the region at ~8983 – 8984 eV, which is commonly considered to be the energy range for the 1s→4p transition in Cu^{I}.[51] However, considering that no intensity loss in the Cu^{II} feature at 8977– 8978 eV was observed and that the decrease of Cu center coordination symmetry upon dehydration, we conclude that Cu remains 100 % as Cu^{II} in the O_2 activated Cu-2.9-NU-1000. Upon exposing Cu-2.9-NU-1000 to 1 bar methane at 150 °C for 180 minutes, the white line as well as the ~8978 eV features are largely unchanged. Only a very small increase in the Cu^{I} 1s→4p transition intensity at ~8983 eV was observed. Linear combination fitting suggested that Cu^{II} remains the dominant state, with a residual fraction of approximate 6% Cu^{I} (Figures S19). The XANES of steam-treated Cu-2.9-NU-1000 (Post) is nearly identical to that of as synthesized samples, indicating that this sample is fully hydrated at the end of the reaction cycle, which is in accordance with the EXAFS curve in Figure 4b.

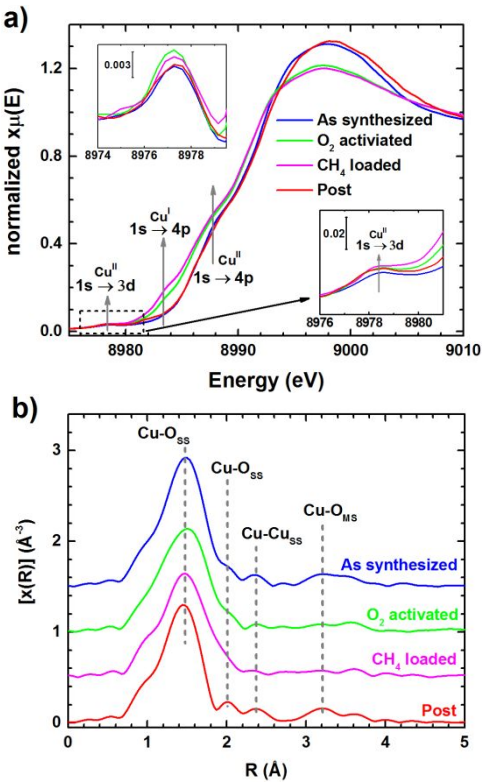

Figure 4. (a) Normalized Cu-XANES and (b) k^2-weighted Cu-EXAFS χ(R) spectra of Cu-2.9-NU-1000 measured during a full cycle of selective methane oxidation to methanol. The top (first derivative χμ(E)) and bottom (normalized χμ(E)) inset show a magnification of pre-edge feature at 8973–8982 eV corresponding to the 1s→3d electronic transition for the Cu^{II}.

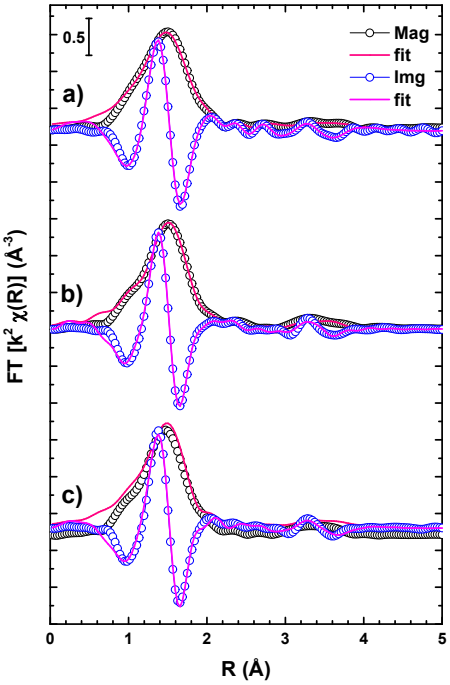

Figure 5. k^2-weighted Cu K-edge Magχ(R) and Imgχ(R) spectra of oxygen activated (a) Cu-2.9-NU-1000, (b) Cu-1.9-

NU-1000, (c) Cu-0.6-NU-1000, and the corresponded FEFF fits.

Table 1. Parameters determined for Cu in Cu-NU-1000 by fitting the experimental spectra with a $Cu(OH)_2$ model derived using FEFF9. [a] Other parameters: amplitude reduction factor (amp) = 0.83 ± 0. 08, R-factor = 0.009, and E0 = -7.6 ± 0.8.

Sample	Path	CN[a]	Distance (Å)	DWF[b]
Cu-2.9-NU-1000	$Cu\text{-}O_{SS}$[c]	4.1±0.2	1.954±0.007	0.0046± 0.0005
	$Cu\text{-}Cu_{SS}$	1.0±0.3	2.871±0.017	0.0111± 0.0024
	$Cu\text{-}O_{MS}$[d]	N/A[e]	3.908±0.014	0.0184± 0.0020
Cu-1.9-NU-1000	$Cu\text{-}O_{SS}$	3.6±0.2	1.960±0.0012	0.0053± 0.0006
	$Cu\text{-}Cu_{SS}$	0.6±0.3	2.844±0.015	0.0169± 0.0069
	$Cu\text{-}O_{MS}$	N/A	3.920±0.0024	0.0212± 0.0010
Cu-0.6-NU-1000	$Cu\text{-}O_{SS}$	3.5±0.6	1.962±0.013	0.0069± 0.0010
	$Cu\text{-}Cu_{SS}$	/ [f]	/	/
	$Cu\text{-}Zr_{SS}$	0.8±0.4	3.603 ±0.033	0.0178± 0.0051
	$Cu\text{-}O_{MS}$	N/A	3.924±0.026	0.0273± 0.0040

[a] CN = average coordination number; [b] DWF = Debye–Waller Factors; [c] SS = single scattering; [d] MS = multiple scattering; [e] NA= not available; [f] Fitting Cu-0.6-NU-1000 with a Cu-Cu path doesn't improve the overall fitting quality, which implies Cu ions are isolated; Fits obtained with k-weighting of 2.

In order to determine the coordination environment of Cu-NU-1000, we fitted the experimental EXAFS spectra of all the three samples, using the $Cu(OH)_2$ model as an initial model. This structure was chosen, because the $Cu(OH)_2$ model contains the minimum set of parameters and the values of these parameters for the $Cu(OH)_2$ reference are closer than that for other Cu(II) references. The best fit is shown in Figures 5 and S21, with all magnitude (Mag), imaginary (Img), and χ (k) plots displayed. The fitted parameters are listed in Table 1. In all samples Cu is coordinated with four O atoms with an average bond distance of 1.95-1.96 Å. Taking into account the ~3.91 Å multiple Cu-O scattering, one can conclude that these four O atoms form a square planar configuration. For Cu-2.9-NU-1000, the fit shows a Cu-Cu path with interatomic distance of 2.87 Å and the coordination number (CN) of 1.0 ± 0.3 consistent with Cu present as a dinuclear cluster. For Cu-1.9-NU-1000 sample, the Cu-Cu CN is 0.6 ± 0.3 suggesting that a fraction of Cu is present as mononuclear. Fitted values for the Cu-Cu parameters of Cu-0.6-NU-1000 were insignificant suggesting that Cu is predominantly present in isolated monomeric structures. Fitting with a Cu–O-Zr path for Cu-2.9-NU-1000 and Cu-1.9-NU-1000 did not significantly improve the fit quality nor changed it the Cu-O and Cu-Cu fit parameters, suggesting Cu-Zr interactions are significantly disordered.[45] However, for Cu-0.6-NU-1000, a Cu-Zr scattering with CN of about 0.8 and bond distance of 3.6 Å was obtained. Thus, it may be that for the samples with higher Cu loading, the Cu-Zr interactions are not detected due to disorder in their structures. Considering the variation in Cu-Cu CNs (Table 1) discussed above, we conclude that the Cu in the Cu-2.9-NU-1000, Cu-1.9-NU-1000 and Cu-0.6-NU-1000 is present as dinuclear Cu, a mixture of dinuclear and mononuclear Cu, and mononuclear Cu, respectively. This hypothesis is supported by the comparison of k^1-, k^2-, and k^3-weighted Img[χ(R)] spectra of Cu-2.9-NU-1000 and Cu-0.6-NU-1000 (Figure S23). The Cu-O peak has been scaled so that their amplitudes are approximately equivalent. As the k-weight increases, the amplitudes of the features between 2.2 and 3.2 Å increase for Cu-2.9-NU-1000, which is indicative of a heavy backscatter (Cu). This effect is very small for Cu-0.6-NU-1000. This hypothesis is also supported by the comparison of FTIR and EPR spectra of these two samples (Figures S9, S11, and Table S1). FTIR results show that the ratios of deposited Cu ions to consumed terminal hydroxyl groups on each Zr_6 nodes are approximately 1:1 for Cu-0.6-NU-1000 and 2:1 for Cu-1.9-NU-1000. Quantification of the paramagnetic signals in EPR spectra suggests that the isolated Cu^{II} species account for 70–80% and 20-30 % of the total Cu species in the Cu-0.6-NU-1000 and Cu-2.9-NU-1000, respectively.

Computed Structures for the Cu sites in Cu-NU-1000

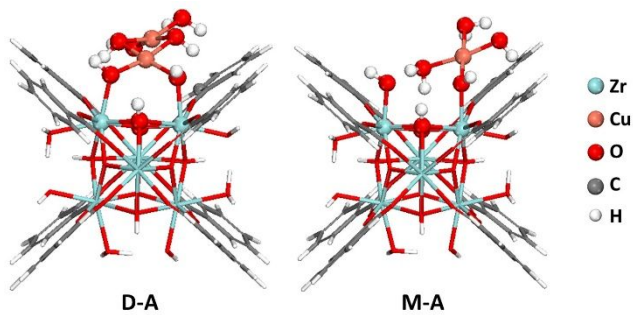

Figure 6. Possible DFT-optimized structure of dinuclear **D-A** complex $[Cu^{II}_2(OH)_4\ (H_2O)]$ on the MOF and and mononuclear **M-A** complex $[Cu^{II}\ (OH)_2\ (H_2O)_2]$ on the MOF.

Given the 4-coordinate square planar $Cu(OH)_2$-like structure determined by EXAFS, we used DFT with the M06-L density functional to compute a series of dinuclear and mononuclear Cu structures as shown in Figures S26 and S28.[28, 61] Optimized dinuclear (**D-A**) and mononuclear (**M-A**) structures that best correspond with the experimental EXAFS data are shown in Figure 6. In the **D-A** structure, the first Cu atom is attached to the Zr_6 node via two Cu-OH(μ_3)-Zr linkages, and the second Cu sits far away from the Zr_6 node bridged to the first Cu atom via another two O atoms. Four O atoms coordinate each Cu ion in a slightly distorted square planner phase. The calculated Cu-Cu distance is 2.80 Å, close to the experimental value of 2.87 Å (Table 1). In the **M-A** structure, a single Cu is attached to the Zr_6 node via a Cu-OH(μ_3)-Zr linkage with Cu-O and Cu-Zr distances of 1.95 and 3.55 Å, respectively, which are in accordance with the EXAFS determined values. The four O atoms show a nearly perfect planar configuration with two O-Cu-O angles at 170.9 and two at 177.3°.

We further compared the experimental EXAFS spectra of Cu-2.9-NU-1000 and Cu-0.6-NU-1000 with spectra simulated by calculating the Cu scattering paths using the **D-A** and **M-A** model structures (Figures 7 and Figures S24, S26). The simulated EXAFS spectra are in good agreement with the respective experiments. Close match of all the $Cu\text{-}O_{SS}$, $Cu\text{-}Cu_{SS}$ (only for **D-A** model), and $Cu\text{-}O_{MS}$ paths in Img[χ(R)] and the oscillation in x(k) confirm that the computationally defined structure are excellent agreement with the fact that the majority of sites is dinuclear.

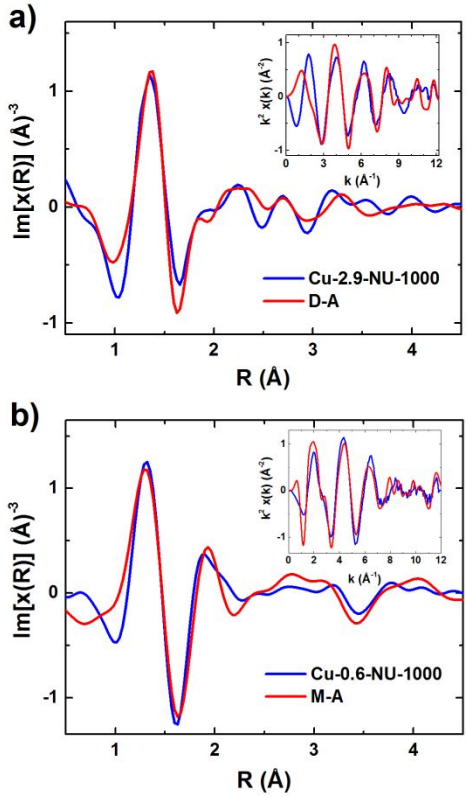

Figure 7. k^2-weighted Cu-EXAFS Img[χ(R)] spectra for (a) Cu-2.9-NU-1000 and (b) Cu-0.6-NU-1000 and the DFT-optimized **D-A** and **M-A** models. Insets show the respective x(k) plots.

Thermodynamic analysis

The relatively low reactivity suggests that active and inactive Cu sites are present after O_2 activation at 200 °C. In order to determine possible structures of the active sites after O_2 activation, a quantum mechanical thermodynamic study has been performed with the M06-L exchange-correlation density functional (the computational details and cluster models of this study and the following study of the reaction mechanism are provided in the computational section and the SI). We started from the structures of the monocopper and dicopper species, $Cu^{II}(OH)_2(H_2O)_2$ (**M-A**) $Cu^{II}_2(OH)_4(H_2O)$ (**D-A**), identified above by DFT and XAFS and shown in Figure 6. These structures are also shown in Figure 8, where we introduce shorthand formula notations and simplified pictorial representations for cluster models to be used in a thermodynamic analysis and a mechanistic exploration. The thermodynamic and mechanistic calculations were carried out with large cluster models illustrated as the left-side figures in panels a, b, c, and d of Figure 8. Two of the cluster models for monocopper and dicopper species before oxygen activation are shown in Figures 8a and 8b, two for the copper oxyl species are shown in Figures 8c and 8d, and the rest are in the SI (Figure S31). Throughout the text and the SI, we use the formulas under the structures in these figures as a shorthand to represent the cluster models. We use the structures on the right side of each panel as pictorial shorthand for those on the left side, but in all cases, the actual calculations include the whole NU-1000 node with four benzoate and four formate linkers as in the left sides of the panels.

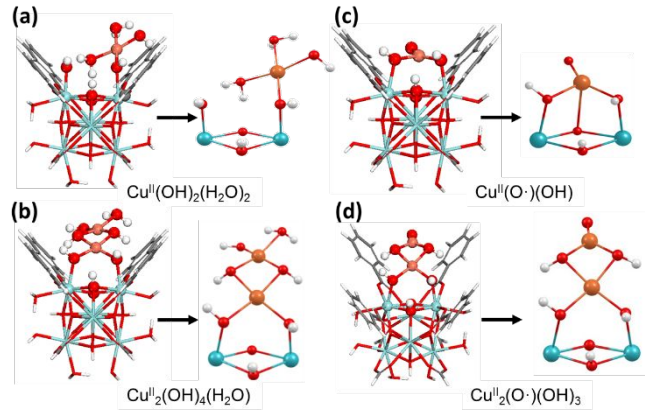

Figure 8. The cluster models for (a) $Cu^{II}(OH)_2(H_2O)_2$, (b) $Cu^{II}_2(OH)_4(H_2O)_2$, (c) ($Cu^{II}(O\cdot)(OH)$ and (d) $Cu^{II}_2(O\cdot)(OH)_3$). The NU-1000 node with the fragment shown in the form of sticks in the left hand column of the figures are ignored to clearly show the structures of copper species in the following sections, which are shown in the right hand column.

First, we calculated the free energies for the following reactions under the activation condition (p_{O_2}=1) to identify the relative stability of the possible Cu species at temperatures ranging from 298 K to 773 K. The results of this analysis are summarized in Figure 9. At the activation temperature (473 K), three cupric ion species, $Cu^{II}(OH)_2$, $Cu^{II}O$, and $Cu^{II}_2(OH)_4$, are predicted to be the most stable species. The calculations indicate that under the activation condition only a small fraction of Cu^{II} was converted to the oxyl species $Cu^{II}(O\cdot)(OH)$ and $Cu^{II}_2(O\cdot)(OH)_3$.

$$\mathrm{Cu}_x(\mathrm{OH})_y(\mathrm{H_2O})_z + \frac{2l+2m-y}{4}\mathrm{O_2} \rightarrow \mathrm{Cu}_x\mathrm{O}_l(\mathrm{OH})_m(\mathrm{H_2O})_n + \frac{y+2z-m-2n}{2}\mathrm{H_2O}$$

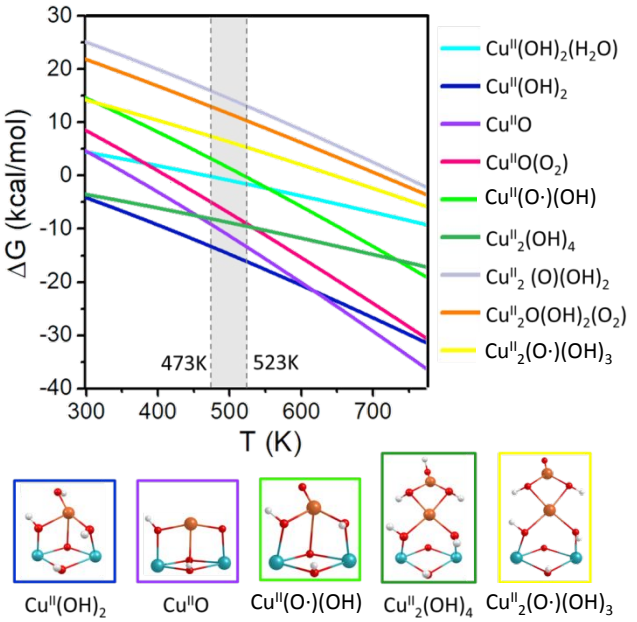

Figure 9. Phase diagram of possible copper species formed under O_2 activation conditions. The bottom of the figure shows the structures of the most dominant species [$Cu^{II}(OH)_2$, $Cu^{II}O$ and $Cu^{II}_2(OH)_4$] in the temperature range of interest (473 K - 523 K) and the two oxyl species [$Cu^{II}(O\cdot)(OH)$ and $Cu^{II}_2(O\cdot)(OH)_3$]. See Figure S31 in the SI for the structures of the full list of investigated species.

Understanding Reaction Mechanism

We also investigated the reaction mechanism for methane oxidation by DFT calculations of free energies of activation for the dominant and possibly active Cu species, with the results shown in Figure 10. The calculations do not take into account the catalyst activation and methanol desorption steps, which are separate processes that require additional steam.

For the cupric hydroxide species, $Cu^{II}(OH)_2$ and $Cu^{II}_2(OH)_4$, Figures 10a and 10d show that the reaction is initiated by homolytic C–H bond dissociation, with H attaching to an OH group to form an H_2O ligand. Then the CH_3 abstracts a OH from the H_2O ligand to produce CH_3OH. The Gibbs free energies of activation for these two steps are very large (39 and 59 kcal/mol for $Cu^{II}(OH)_2$, 35 and 47 kcal/mol for $Cu^{II}_2(OH)_4$), suggesting their low activity for methane oxidation.

Dehydration of $Cu^{II}(OH)_2$ and $Cu^{II}_2(OH)_4$ could potentially generate $Cu^{II}O$ and $Cu^{II}_2O(OH)_2$, respectively. Methane oxidation on by $Cu^{II}O$ follows a similar pathway to that on $Cu^{II}(OH)_2$, and it shows better activity than $Cu^{II}(OH)_2$ (Figure 10b) because of the smaller free energy barriers (33 and 59 kcal/mol). Figure 10e shows that for $Cu^{II}_2O(OH)_2$, the reaction is again initiated by homolytic C–H bond dissociation, but now the H atom attaches to the oxyl to form an OH ligand. Then the CH_3 abstracts OH from Cu to produce CH_3OH. This reaction of OH and CH_3, adsorbed at the same Cu ion, is much more facile than abstraction of OH from H_2O, and the free energy of activation is much lower. The Gibbs free energies of activation for the two steps (Figure 10e) decrease to 23 kcal/mol (smaller than for the dinuclear Cu cluster studied previously[31]) and 38 kcal/mol, indicating better activity than $Cu^{II}O$. We noted that the triplet spin state for $Cu^{II}_2O(OH)_2$ is preserved for the first step, and the product of second step is a closed-shell ground state, so the reaction involves a spin-changing transition.[62-63]

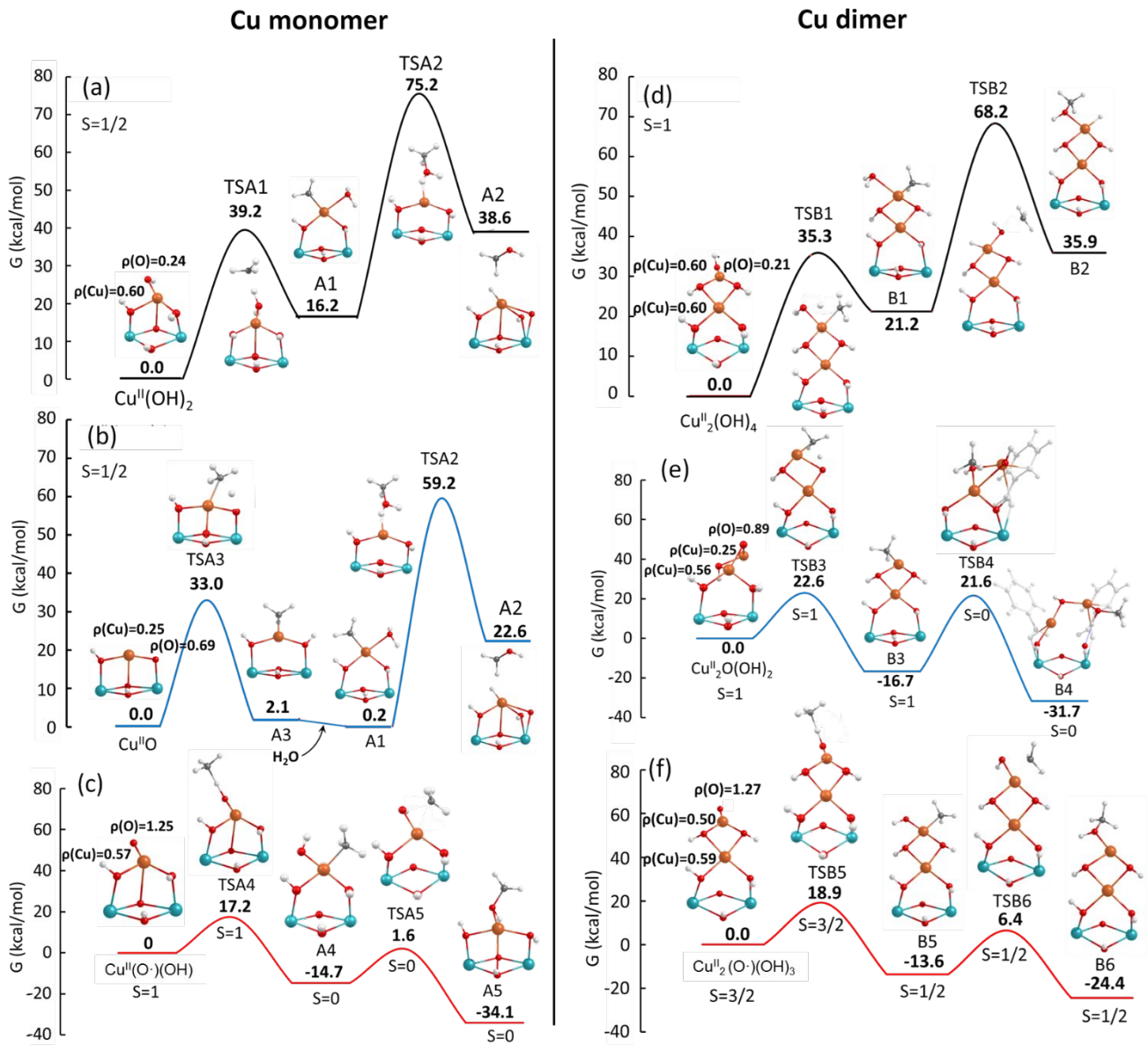

Figure 10. The reaction mechanisms of methane oxidation over possible active copper sites for (a) $Cu^{II}(OH)_2$, (b) $Cu^{II}O$, (c) $Cu^{II}(O\cdot)(OH)$, (d) $Cu^{II}_2(OH)_4$, (e) $Cu^{II}_2O(OH)_2$, and (f) $Cu^{II}_2(O\cdot)(OH)_3$. The quantities shown are free energies of equilibrium species and free energies of activation of transition states, both relative to the leftmost species in the given panel. All results are for a temperature of 298 K and a pressure of 1 bar. Illustrative atomic spin densities of the initial catalyst are shown in the figure, where they are labeled ρ; *S* is the total electron spin. The doublet spin state of $Cu^{II}(OH)_2$ and the triplet spin state of $Cu^{II}_2(OH)_4$ are preserved along the reaction path, and in these cases the spin density is mainly localized at Cu atoms for all the structures along the pathway. For the triplet case, the spin coupling of the Cu centers is ferromagnetic. However, as shown in the figure, in some cases the spin quantum number of the lowest-energy species is not the same for all structures on a given path.

Even though, copper oxyl species $Cu^{II}(O\cdot)(OH)$ and $Cu^{II}_2(O\cdot)(OH)_3$) are predicted by our thermodynamic analysis to be present in relative small quantities, the Gibbs free energy profiles shown in Figures 10c and 10f suggest their high activity for methane oxidation to produce methanol. The calculated free energy of activation for the first step is 17.2 kcal/mol and 18.9 kcal/mol, respectively for $Cu^{II}(O\cdot)(OH)$ and $Cu^{II}_2(O\cdot)(OH)_3$, which are comparable to the previously reported values on Cu/zeolite or Cu/porphyrin systems.[15, 64-66] The rebounding of the CH_3 from Cu to OH is exergonic by 19 and 11 kcal/mol for $Cu^{II}(O\cdot)(OH)$ and $Cu^{II}_2(O\cdot)(OH)_3$ respectively. Subsequently, the CH_3 abstracts the geminal OH bound leading to the formation CH_3OH with an free energy

barrier 16 kcal/mol for $Cu^{II}(O\cdot)(OH)$ and 20 kcal/mol for $Cu^{II}_2(O\cdot)(OH)_3$.

The reaction paths showed in Figures 10c and 10f also involve spin transitions. We found that the activity of the Cu species increases with the increase of spin density of O, which is consistent with previous studies.[31]The high activity of the copper oxyl species [for example, $Cu^{II}(O\cdot)(OH)$] may be understand either in terms of the existence of an active oxygen or the higher oxidizing power of a Cu that can be regarded as a Cu^{III}-oxo.[67-69]

The calculations indicate that the cupric hydroxide species, $Cu^{II}(OH)_2$ and $Cu^{II}_2(OH)_4$, which are predicted to be the dominant species, have large free energies of activation and therefore very low activity for the methane-to-methanol reaction, but the minority copper oxyl species are the active sites for methane to methanol. We conclude that the overall low activity of Cu-NU-1000 is due to the small concentration of the active oxyl species. These observations are consistent with the experimental results.

In addition, the mononuclear $Cu^{II}(O\cdot)(OH)$ is found to be as active as the dinuclear $Cu^{II}_2(O\cdot)(OH)_3$ for methane to methanol reaction, which implies, if the catalyst contains only the two copper oxyl species that we identified, that the methanol yield should be found to be linearly related to the Cu loading. However the methanol yields are 9.7 and 1.4 $mmol_{MeOH}/mol_{Cu}$ for Cu-2.9-NU-1000 and Cu-0.6-NU-1000, respectively, which are not linearly related to the Cu loading. This observation suggests several possibilities. (1) $Cu^{II}_2O(OH)_2$, which is more active than $Cu^{II}O$, may also be involved in the reaction, leading to the increase the methanol yield for Cu-2.9-NU-1000. (2) The identified **M-A** structure for the monocopper species has a relatively low stability and diffuses to and reacts with the linker,[16] reducing the number of active sites for Cu-0.6-NU-1000.

Structure-Activity Discussion

The *in situ* XAS, FTIR, and EPR characterizations and DFT calculations confirmed the presence of dinuclear and mononuclear copper sites on the Cu-exchanged NU-1000 MOFs. The methanol productivity per Cu atom of dicopper-dominated Cu-2.9-NU-1000 is 6.4-fold higher than that of monomer-dominated Cu-0.6-NU-1000 (1 bar methane and 150 ºC). Thus, we conclude that the dinuclear copper oxyl species is the main contributor for methane oxidation over Cu-exchanged NU-1000.

The active sites are generated during the oxygen activation step at 200 ºC. After activation, there is a partial dehydration of the hydroxyl species, but the overall structure of the dinuclear Cu clusters does not change, which was confirmed by a control experiment, where methanol was not produced on the same material without an oxygen activation step. These results allow us to conclude that dinuclear and mononuclear Cu sites are formed during synthesis, which are precursors of the active site, since the heat treatment only removes water, but does not change the nuclearity of the Cu sites. The computational thermodynamic analysis corroborates the existence of different types of dinuclear Cu sites after O_2 activation at 200 ºC, e.g., Cu "dry" oxyl-like and "hydrated" cupric hydroxide-like species, the latter being the most stable component in the material (in agreement with its high abundance found by EXAFS analysis). DFT calculation demonstrate that copper oxyl species are active for selective methane oxidation. However, the dominant Cu hydroxide-like species are less active.

At 150 °C and 1 bar methane, the formation of 9.7 mmol methanol requires that 19.4 mmol Cu is reduced from Cu^{II} to Cu^{I}, which is approximately 2 % of all Cu in Cu-2.9-NU-1000. We observed, however, about 6 % of Cu^{II} was consistently reduced to Cu^{I} during methane exposure (*in situ* XANES spectra), i.e., three times more than needed for methanol production. Thus, only a third of the reactive Cu centers is involved in the selective methane oxidation to methanol under these conditions. The other two thirds of reacting Cu^{II} are involved in CO_2 production, which requires eight electrons. While, at 200 °C and 40 bar methane, the formation of ~38.8 mmol methanol (include 2 mmol DME) and 4.3 mmol CO_2 requires that 78 and 34.4 mmol Cu is reduced from Cu(II) to Cu(I), respectively. In another word, about 70% of the reactive Cu centers is involved in the selective methane oxidation to methanol.

Overall, the activities of MOF-based materials for methane oxidation are lower than those of Cu-zeolites. The latter, however, are typically activated at temperatures of up to 500 °C, which is important for the formation of active $(Cu–O–Cu]^{2+}$ or $[Cu_3(\mu\text{-}O)_3]^{2+}$.[13-14, 70] Due to the thermal stability limit of MOFs, they have been activated at the milder temperatures of 150–200 °C, which leads to a comparatively small fraction of active sites. As an alternative strategy, here we found that increasing the pressure of methane increases the methane conversion and the methanol selectivity on Cu-exchanged NU-1000. The reasons of the enhancing effect of the high methane pressure is not clear yet. We hypothesize that either the coverage of active molecular species increases, or to enabling additional Cu sites to activate methane. A detailed kinetic and mechanic study to understand how the methane pressure affect the productivity of methanol and the distribution of products is ongoing.

CONCLUSION

Using a liquid phase post-synthetic cation-exchange, 0.6–2.9 wt % Cu was successfully anchored in nodes of NU-1000 MOF. X-ray adsorption spectroscopy suggests that Cu in the as-synthesized MOFs has a local structure similar to Cu in a fully hydrated $Cu(OH)_2$. Heating the MOFs in oxygen at 200 °C does not change the overall structure and oxidation state of Cu, but leads to the dehydration of Cu centers. The data also show that, whereas the MOF with highest loading of Cu contained mainly dinuclear Cu, the MOF with lowest Cu loading contained predominantly mononuclear Cu. DFT calculations of the Cu species are in good agreement with experiments and thus lend confidence to our interpretation of the data. The dinuclear species is predicted to have one Cu attached to the Zr_6 node via two μ_3-OH groups and a second Cu that sits far away from the Zr_6 node, bridged to the first Cu atom via two μ-OH groups. Evaluation of the resulting material for methane oxidation to methanol showed that the

MOF with highest amount of Cu is 6.4 times more productive per Cu than the MOF with lowest loading. Combined with the stoichiometric activity, *in situ* structural characterization, and density functional theory, we conclude that dinuclear copper oxyl centers are responsible for the observed high selectivity (~ 70%) to methanol. The sample gives a higher methanol yield (3-4 fold) and higher methanol selectivity (~90%) by increasing methane pressure from 1 bar to 40 bar. This implies that about 11.2 mol % of Cu in the material is involved in methane activation, which, to the best of our knowledge, might be the highest value on MOF-based materials to date.

EXPERIMENTAL SECTION

Chemicals

High-purity (99.995%) helium, oxygen, and methane were purchased from Matheson. Methane-^{13}C (99%) and Copper acetate (99.99%) were obtained from Sigma-Aldrich. All water was provided by a Mini-Q Plus water purification system (Millipore). All the chemicals were used as received.

Materials Syntheses

The NU-1000 MOF was synthesized via a solvent thermal reaction at 120°C, similar to the literature procedure reported elsewhere.[71] Cu-NU-1000 samples were synthesized via an ion-exchange route in aqueous solution under ambient condition. Copper acetate was chosen as the Cu precursor. In a typical experiment, 0.5 g NU-1000 (0.23 mmol) was mixed with 300 ml of 0.001 to 0.01 M Copper acetate solution. The measured pH values of the solution were 5.0–6.0 during exchange. A typical exchange time was 24 h. After exchange, the product was washed with deionized water at least 3 times and separated by centrifugation. After the last water washing, the sample was suspended in 50 ml acetone for 12 hours to allow solvent exchange. This step was repeated for 3 times. The solvent exchanged sample was then collected and dried in vacuum oven overnight at 120 °C. The concentration of Cu in Cu-NU-1000 samples was determined from inductively coupled plasma–atomic emission spectroscopy (ICP-AES) measurements.

XAS Measurements

The XANES and EXAFS experiments took place at the Pacific Northwest Consortium/X-ray Science Division (PNC/XSD) bending-magnet beamline at Sector 20 of the Advanced Photon Source (APS) at Argonne National Laboratory (ANL). Same to previous report,[45] all experiments were carried out in transmission mode with a focused beam (0.7 × 0.6 mm) delivering 10^{10} photons through the sample. A harmonic rejection mirror was used to reduce the effects of harmonics. A Cu foil was placed downstream of the sample cell, as a reference to calibrate the photon energy of each spectrum. The XAFS reaction cell is based on a HiP medium-pressure Hastelloy tee modified to house the four-sample holder and allow gas flow-through capability.[45] Glassy-carbon discs (thickness = 0.75 mm, diameter = 5 mm) were used as the X-ray windows. The Cu-NU-1000 samples were pressed (0.25 ton) into pellets that were 0.5 to 2.0 mm thick. Prior to data acquisition, all gas lines were purged with dry He, and then with dry O_2 or CH_4, for activation and loading, respectively. A flow rate of 2.5 mL/min was used during data acquisition. Data analysis and background removal were performed using ATHENA and ARTEMIS programs from the iXAFS software package.[72] The Fourier transform of the k-space EXAFS data were fitted to theoretical models derived using the FEFF9 code.[73]

EXAFS spectra simulation

EXAFS spectra of DFT-optimized Cu clusters were simulated using ab initio scattering theory by applying approximate global disorder parameters($\sigma 2$), corresponding to 300 K. The computed coordinates were used to generate the primary input for the ab initio EXAFS scattering code (FEFF9)[73] that includes all the single and multiple scattering paths out to 6 Å, resulting in several hundred scattering paths for each Cu atom in the structure. An approximate treatment of the bond disorder at 300 K is applied by setting a universal value of the DWF, $\sigma 2 = 0.005$. The obtained spectra for each Cu atom in the cluster are then averaged, and an overall E_0 is applied to match experimental values (oscillations in $\chi(k)$ converge at k = 0). While the global DWF is a good estimate of the first shell disorder, it is an overestimation of the order in the higher shells which manifests as an over-prediction of these amplitudes, although the atom positions predicted by the theory are correctly represented.

Thermogravimetric Analysis (TGA)

TGA and differential scanning calorimetry (TG-DSC) analyses were performed on a SENSYS EVO TG-DSC (SETARAM Instrumentation) at the ramp rate of 3 K/min.

N_2-Sorption

N_2-physisorption for surface area and pore volumes was obtained on a Micromeritics ASAP 2020 instrument. The carbon slit pore model with a NL-DFT method was used. Single-point adsorption close to P/P0 = 0.99 was used to determine the total pore volume.

In situ FTIR

Infrared spectra of the MOFs were recorded on a ThermoScientific Nicolete FTIR spectrometer equipped with CaF_2 windows and a MCT detector with a resolution of 4 cm^{-1}. 128 scans were accumulated for each spectrum. The samples for IR measurements were prepared as self-supporting thin wafers with a density of approximately 2-3 mg/cm^2. Upon loading in the IR-cell, the samples were evacuated to 1.0×10^{-6} mbar at 150 ºC for 2 hours. The spectra were collected after the cell cooled to room temperature.

Powder X-ray Diffraction (PXRD)

PXRD patterns of Cu-NU-1000 were recorded on EMPYREAN (PANalytical) with Cu Kα radiation (λ = 1.5406 Å, 45 kV, 40 mA).

Transmission Electron Microscopy (TEM)

The samples were infiltrated in LR White acrylic resin (Electron Microscopy Sciences, Hatfield, PA) and polymerized at 60 °C for 24 h. The embedded material was sectioned to a 50 nm thickness on Leica ultramicrotome (Ultracut E) using a Diatome diamond knife. The microtomed samples were placed on 200-mesh lacey-carbon-coated Cu grids (Ted Pella) and imaged with an aberration-corrected

JEOL 200F operating at 200 keV. The HAADF nominal probe size was ~0.1 nm.

Catalytic Testing

The activity of Cu-NU-1000 for methane oxidation to methanol was tested either at atmospheric or elevated pressure. The reaction was performed in a stainless-steel plug flow reactor with a 4 mm inner diameter. The catalytic reaction included three consecutive steps: (1) sample activation in O_2, (2) CH_4 loading, and (3) water-steam purge necessary for product desorption. Typically, 50 - 200 mg of Cu-exchanged NU-1000 was loaded in the reactor and activated in O_2 flow (16 mL min^{-1}) at 200 °C, followed by flushing in He. Pure CH_4 was flown subsequently in the flow of 16 mL min^{-1} h at 150 or 200 °C for 3 h. After cooling to 135 °C in He flow, steam-assisted product desorption was performed in 10/90 (molar) mixture of H_2O/He purged at a flow rate of 20 mL/min for up to 3 h. The oxidation products were identified and quantified using online mass spectrometry and by monitoring the time-dependent evolution of signals at m/z of 31, 44 and 46, characteristic for methanol, CO_2 and dimethyl ether, respectively. The He signal (m/z = 4) was used as an internal standard.

Computational Section

All density functional calculations in this work were performed using the M06-L density functional[61] as implemented in *Gaussian 09*.[74] The M06-L functional has shown good performance for me-dium-range electron-correlation effects, transition metal chemistry,[75] and MOF-supported catalysts.[31, 45]

The thermodynamic and mechanistic calculations were carried out with cluster models containing one NU-1000 node with four benzoate and four formate linkers. During optimization all atoms were relaxed while the carbon atoms were kept fixed. The other computational details are given in the SI.

Unrestricted density

ASSOCIATED CONTENT

Supporting Information

The Supporting Information is available free of charge on the ACS Publications website. Schematic setup for catalytic testing, PXRD, SEM, TEM, N_2-sorption, FTIR, EPR, MS characterizations, details of XAFS fitting analysis, DFT-optimized models, and Cartesian coordinates, including Figures S1–S33 and Tables S1–S7 (PDF).

AUTHOR INFORMATION

Corresponding Author

*johannes.lercher@pnnl.gov, johannes.lercher@ch.tum.de

Author Contributions

⊗J.Z., and J.Y. contributed equally.

ACKNOWLEDGMENT

The authors gratefully acknowledge support for this work from the Inorganometallic Catalyst Design Center, an EFRC funded by the U.S. Department of Energy (DOE), Office of Science, Office of Basic Energy Sciences (DE-SC0012702). This research used resources of the APS, which is a DOE Office of Science, Office of Basic Energy Sciences User Facility. Sector 20 operations at the APS are supported by the U.S. DOE (DE-AC02-06CH11357) and the Canadian Light Source. We thank Dr. Mahalingam Balasubramanian (APS X-ray Science Division) for assisting in the XAFS experiments. Most of the experiments were performed at Pacific Northwest National Laboratory (PNNL), a multi-program national laboratory operated by Battelle for the U.S. DOE. We also acknowledge the Minnesota Supercomputing Institute (MSI) at the University of Minnesota for providing resources that contributed to the research results reported within this paper.

REFERENCES

(1) Guo, X. G.; Fang, G. Z.; Li, G.; Ma, H.; Fan, H. J.; Yu, L.; Ma, C.; Wu, X.; Deng, D. H.; Wei, M. M.; Tan, D. L.; Si, R.; Zhang, S.; Li, J. Q.; Sun, L. T.; Tang, Z. C.; Pan, X. L.; Bao, X. H. Direct, Nonoxidative Conversion of Methane to Ethylene, Aromatics, and Hydrogen, *Science* **2014,** *344*, 616-619.

(2) Caballero, A.; Perez, P. J. Methane as raw material in synthetic chemistry: the final frontier, *Chem Soc Rev* **2013,** *42*, 8809-8820.

(3) Chan, S. I.; Yu, S. S. F. Controlled oxidation of hydrocarbons by the membrane-bound methane monooxygenase: The case for a tricopper cluster, *Accounts Chem Res* **2008,** *41*, 969-979.

(4) Chan, S. I.; Lu, Y. J.; Nagababu, P.; Maji, S.; Hung, M. C.; Lee, M. M.; Hsu, I. J.; Minh, P. D.; Lai, J. C. H.; Ng, K. Y.; Ramalingam, S.; Yu, S. S. F.; Chan, M. K. Efficient Oxidation of Methane to Methanol by Dioxygen Mediated by Tricopper Clusters, *Angew Chem Int Edit* **2013,** *52*, 3731-3735.

(5) Liu, C. C.; Mou, C. Y.; Yu, S. S. F.; Chan, S. I. Heterogeneous formulation of the tricopper complex for efficient catalytic conversion of methane into methanol at ambient temperature and pressure, *Energ Environ Sci* **2016,** *9*, 1361-1374.

(6) Tomkins, P.; Ranocchiari, M.; van Bokhoven, J. A. Direct Conversion of Methane to Methanol under Mild Conditions over Cu-Zeolites and beyond, *Accounts Chem Res* **2017,** *50*, 418-425.

(7) Sushkevich, V. L.; Palagin, D.; Ranocchiari, M.; van Bokhoven, J. A. Selective anaerobic oxidation of methane enables direct synthesis of methanol, *Science* **2017,** *356*, 523-527.

(8) Starokon, E. V.; Parfenov, M. V.; Arzumanov, S. S.; Pirutko, L. V.; Stepanov, A. G.; Panov, G. I. Oxidation of methane to methanol on the surface of FeZSM-5 zeolite, *J Catal* **2013,** *300*, 47-54.

(9) Kulkarni, A. R.; Zhao, Z. J.; Siahrostami, S.; Norskov, J. K.; Studt, F. Cation-exchanged zeolites for the selective oxidation of methane to methanol, *Catal Sci Technol* **2018,** *8*, 114-123.

(10) Pappas, D. K.; Borfecchia, E.; Dyballa, M.; Pankin, I. A.; Lomachenko, K. A.; Martini, A.; Signorile, M.; Teketel, S.; Arstad, B.; Berlier, G.; Lamberti, C.; Bordiga, S.; Olsbye, U.; Lillerud, K. P.; Svelle, S.; Beato, P. Methane to Methanol: Structure Activity Relationships for Cu-CHA, *J Am Chem Soc* **2017,** *139*, 14961-14975.

(11) Kim, Y.; Kim, T. Y.; Lee, H.; Yi, J. Distinct activation of Cu-MOR for direct oxidation of methane to methanol, *Chem Commun* **2017,** *53*, 4116-4119.

(12) Narsimhan, K.; Iyoki, K.; Dinh, K.; Roman-Leshkov, Y. Catalytic Oxidation of Methane into Methanol over Copper-Exchanged Zeolites with Oxygen at Low Temperature, *Acs Central Sci* **2016,** *2*, 424-429.

(13) Groothaert, M. H.; Smeets, P. J.; Sels, B. F.; Jacobs, P. A.; Schoonheydt, R. A. Selective oxidation of methane by the bis(mu-oxo)dicopper core stabilized on ZSM-5 and mordenite zeolites, *J. Am. Chem. Soc.* **2005,** *127*, 1394-1395.

(14) Grundner, S.; Markovits, M. A. C.; Li, G.; Tromp, M.; Pidko, E. A.; Hensen, E. J. M.; Jentys, A.; Sanchez-Sanchez, M.; Lercher, J. A. Single-site trinuclear copper oxygen clusters in mordenite for selective conversion of methane to methanol, *Nat Commun* **2015,** *6*, 7456

(15) Li, G. N.; Vassilev, P.; Sanchez-Sanchez, M.; Lercher, J. A.; Hensen, E. J. M.; Pidko, E. A. Stability and reactivity of copper oxo-clusters in ZSM-5 zeolite for selective methane oxidation to methanol, *J. Catal.* **2016,** *338*, 305-312.

(16) Kulkarni, A. R.; Zhao, Z. J.; Siahrostami, S.; Norskov, J. K.; Studt, F. Monocopper Active Site for Partial Methane Oxidation in Cu-Exchanged 8MR Zeolites, *Acs Catalysis* **2016,** *6*, 6531-6536.

(17) Tomkins, P.; Mansouri, A.; Bozbag, S. E.; Krumeich, F.; Park, M. B.; Alayon, E. M. C.; Ranocchiari, M.; van Bokhoven, J. A. Isothermal Cyclic Conversion of Methane into Methanol over Copper-Exchanged Zeolite at Low Temperature, *Angew Chem Int Edit* **2016,** *55*, 5467-5471.

(18) Farha, O. K.; Eryazici, I.; Jeong, N. C.; Hauser, B. G.; Wilmer, C. E.; Sarjeant, A. A.; Snurr, R. Q.; Nguyen, S. T.; Yazaydin, A. O.; Hupp, J. T. Metal-Organic Framework Materials with Ultrahigh Surface Areas: Is the Sky the Limit?, *J Am Chem Soc* **2012,** *134*, 15016-15021.

(19) Deria, P.; Mondloch, J. E.; Karagiaridi, O.; Bury, W.; Hupp, J. T.; Farha, O. K. Beyond post-synthesis modification: evolution of metal-organic frameworks via building block replacement, *Chem Soc Rev* **2014,** *43*, 5896-5912.

(20) Zheng, J.; Vemuri, R. S.; Estevez, L.; Koech, P. K.; Vargas, T.; Camaioni, D. M.; Blake, T. A.; McGrail, B. P.; Motkuri, R. K. Pore-Engineered Metal-Organic Frameworks with Excellent Adsorption of Water and Fluorocarbon Refrigerant for Cooling Applications, *J Am Chem Soc* **2017,** *139*, 10601-10604.

(21) Deng, H. X.; Grunder, S.; Cordova, K. E.; Valente, C.; Furukawa, H.; Hmadeh, M.; Gandara, F.; Whalley, A. C.; Liu, Z.; Asahina, S.; Kazumori, H.; O'Keeffe, M.; Terasaki, O.; Stoddart, J. F.; Yaghi, O. M. Large-Pore Apertures in a Series of Metal-Organic Frameworks, *Science* **2012,** *336*, 1018-1023.

(22) Zhou, H. C.; Long, J. R.; Yaghi, O. M. Introduction to Metal-Organic Frameworks, *Chem Rev* **2012,** *112*, 673-674.

(23) Yang, D.; Ortuno, M. A.; Bernales, V.; Cramer, C. J.; Gagliardi, L.; Gates, B. C. Structure and Dynamics of Zr6O8 Metal-Organic Framework Node Surfaces Probed with Ethanol Dehydration as a Catalytic Test Reaction, *J Am Chem Soc* **2018,** *140*, 3751-3759.

(24) Cohen, S. M. The Postsynthetic Renaissance in Porous Solids, *J Am Chem Soc* **2017,** *139*, 2855-2863.

(25) Zheng, J.; Barpaga, D.; Gutiérrez, O. Y.; Browning, N. D.; Mehdi, B. L.; Farha, O. K.; Lercher, J. A.; McGrail, B. P.; Motkuri, R. K. Exceptional Fluorocarbon Uptake with Mesoporous Metal–Organic Frameworks for Adsorption-Based Cooling Systems, *ACS Applied Energy Materials* **2018,** *1*, 5853-5858.

(26) Rogge, S. M. J.; Bavykina, A.; Hajek, J.; Garcia, H.; Olivos-Suarez, A. I.; Sepulveda-Escribano, A.; Vimont, A.; Clet, G.; Bazin, P.; Kapteijn, F.; Daturi, M.; Ramos-Fernandez, E. V.; Xamena, F. X. L. I.; Van Speybroeck, V.; Gascon, J. Metal-organic and covalent organic frameworks as single-site catalysts, *Chem. Soc. Rev.* **2017,** *46*, 3134-3184.

(27) Xiao, D. J.; Bloch, E. D.; Mason, J. A.; Queen, W. L.; Hudson, M. R.; Planas, N.; Borycz, J.; Dzubak, A. L.; Verma, P.; Lee, K.; Bonino, F.; Crocella, V.; Yano, J.; Bordiga, S.; Truhlar, D. G.; Gagliardi, L.; Brown, C. M.; Long, J. R. Oxidation of ethane to ethanol by N2O in a metal-organic framework with coordinatively unsaturated iron(II) sites, *Nat. Chem.* **2014,** *6*, 590-595.

(28) Bernales, V.; Ortuno, M. A.; Truhlar, D. G.; Cramer, C. J.; Gagliardi, L. Computational Design of Functionalized Metal-Organic Framework Nodes for Catalysis, *ACS Cent. Sci.* **2018,** *4*, 5-19.

(29) Verma, P.; Vogiatzis, K. D.; Planas, N.; Borycz, J.; Xiao, D. J.; Long, J. R.; Gagliardi, L.; Truhlar, D. G. Mechanism of Oxidation of Ethane to Ethanol at Iron(IV)-Oxo Sites in Magnesium-Diluted Fe-2(dobdc), *J. Am. Chem. Soc.* **2015,** *137*, 5770-5781.

(30) Liao, P. L.; Getman, R. B.; Snurr, R. Q. Optimizing Open Iron Sites in Metal-Organic Frameworks for Ethane Oxidation: A First-Principles Study, *Acs Appl Mater Inter* **2017,** *9*, 33484-33492.

(31) Pahls, D. R.; Ortuno, M. A.; Winegar, P. H.; Cramer, C. J.; Gagliardi, L. Computational Screening of Bimetal-Functionalized Zr6O8 MOF Nodes for Methane C-H Bond Activation, *Inorg. Chem.* **2017,** *56*, 8739-8743.

(32) Simons, M. C.; Ortuno, M. A.; Bernales, V.; Gaggioli, C. A.; Cramer, C. J.; Bhan, A.; Gagliardi, L. C-H Bond Activation on Bimetallic Two-Atom Co-M Oxide Clusters Deposited on Zr-Based MOF Nodes: Effects of Doping at the Molecular Level, *Acs Catalysis* **2018,** *8*, 2864-2869.

(33) Vitillo, J. G.; Bhan, A.; Cramer, C. J.; Lu, C. C.; Gagliardi, L. Quantum Chemical Characterization of Structural Single Fe(II) Sites in MIL-Type Metal Organic Frameworks for Oxidation of Methane to Methanol and Ethane to Ethanol, *ACS Catalysis* **2019**, *9*, 2870-2879

(34) Szecsenyi, A.; Li, G. N.; Gascon, J.; Pidko, E. A. Unraveling reaction networks behind the catalytic oxidation of methane with H2O2 over a mixed-metal MIL-53(Al,Fe) MOF catalyst, *Chem. Sci.* **2018,** *9*, 6765-6773

(35) Beyzavi, M. H.; Vermeulen, N. A.; Howarth, A. J.; Tussupbayev, S.; League, A. B.; Schweitzer, N. M.; Gallagher, J. R.; Platero-Prats, A. E.; Hafezi, N.; Sarjeant, A. A.; Miller, J. T.; Chapman, K. W.; Stoddart, J. F.; Cramer, C. J.; Hupp, J. T.; Farha, O. K. A Hafnium-Based Metal-Organic Framework as a Nature-Inspired Tandem Reaction Catalyst, *J. Am. Chem. Soc.* **2015,** *137*, 13624-13631.

(36) Manna, K.; Ji, P. F.; Lin, Z. K.; Greene, F. X.; Urban, A.; Thacker, N. C.; Lin, W. B. Chemoselective single-site Earth-abundant metal catalysts at metal-organic framework nodes, *Nat. Comm.* **2016,** *7*, 12610

(37) Baek, J.; Rungtaweevoranit, B.; Pei, X. K.; Park, M.; Fakra, S. C.; Liu, Y. S.; Matheu, R.; Alshmimri, S. A.; Alshehri, S.; Trickett, C. A.; Somorjai, G. A.; Yaghi, O. M. Bioinspired Metal-Organic Framework Catalysts for Selective Methane Oxidation to Methanol, *J. Am. Chem. Soc.* **2018,** *140*, 18208-18216.

(38) Mondloch, J. E.; Bury, W.; Fairen-Jimenez, D.; Kwon, S.; DeMarco, E. J.; Weston, M. H.; Sarjeant, A. A.; Nguyen, S. T.; Stair, P. C.; Snurr, R. Q.; Farha, O. K.; Hupp, J. T. Vapor-Phase

Metalation by Atomic Layer Deposition in a Metal-Organic Framework, *J Am Chem Soc* **2013,** *135*, 10294-10297.

(39) Rimoldi, M.; Bernales, V.; Borycz, J.; Vjunov, A.; Gallington, L. C.; Platero-Prats, A. E.; Kim, I. S.; Fulton, J. L.; Martinson, A. B. F.; Lercher, J. A.; Chapman, K. W.; Cramer, C. J.; Gagliardi, L.; Hupp, J. T.; Farha, O. K. Atomic Layer Deposition in a Metal-Organic Framework: Synthesis, Characterization, and Performance of a Solid Acid, *Chem Mater* **2017,** *29*, 1058-1068.

(40) Howarth, A. J.; Katz, M. J.; Wang, T. C.; Platero-Prats, A. E.; Chapman, K. W.; Hupp, J. T.; Farha, O. K. High Efficiency Adsorption and Removal of Selenate and Selenite from Water Using Metal-Organic Frameworks, *J Am Chem Soc* **2015,** *137*, 7488-7494.

(41) Li, Z.; Schweitzer, N. M.; League, A. B.; Bernales, V.; Peters, A. W.; Getsoian, A.; Wang, T. C.; Miller, J. T.; Vjunov, A.; Fulton, J. L.; Lercher, J. A.; Cramer, C. J.; Gagliardi, L.; Hupp, J. T.; Farha, O. K. Sintering-Resistant Single-Site Nickel Catalyst Supported by Metal Organic Framework, *J Am Chem Soc* **2016,** *138*, 1977-1982.

(42) Platero-Prats, A. E.; League, A. B.; Bernales, V.; Ye, J. Y.; Gallington, L. C.; Vjunov, A.; Schweitzer, N. M.; Li, Z. Y.; Zheng, J.; Mehdi, B. L.; Stevens, A. J.; Dohnalkova, A.; Balasubramanian, M.; Farha, O. K.; Hupp, J. T.; Browning, N. D.; Fulton, J. L.; Camaioni, D. M.; Lercher, J. A.; Truhlar, D. G.; Gagliardi, L.; Cramer, C. J.; Chapman, K. W. Bridging Zirconia Nodes within a Metal-Organic Framework via Catalytic Ni-Hydroxo Clusters to Form Heterobimetallic Nanowires, *J Am Chem Soc* **2017,** *139*, 10410-10418.

(43) Desai, S. P.; Ye, J.; Zheng, J.; Ferrandon, M. S.; Webber, T. E.; Platero-Prats, A. E.; Duan, J.; Garcia-Holley, P.; Camaioni, D. M.; Chapman, K. W.; Delferro, M.; Farha, O. K.; Fulton, J. L.; Gagliardi, L.; Lercher, J. A.; Penn, R. L.; Stein, A.; Lu, C. C. Well-Defined Rhodium–Gallium Catalytic Sites in a Metal–Organic Framework: Promoter-Controlled Selectivity in Alkyne Semihydrogenation to E-Alkenes, *J. Am. Chem. Soc.* **2018,** *140*, 15309-15318.

(44) Kim, I. S.; Li, Z. Y.; Zheng, J.; Platero-Prats, A. E.; Mavrandonakis, A.; Pellizzeri, S.; Ferrandon, M.; Vjunov, A.; Gallington, L. C.; Webber, T. E.; Vermeulen, N. A.; Penn, R. L.; Getman, R. B.; Cramer, C. J.; Chapman, K. W.; Camaioni, D. M.; Fulton, J. L.; Lercher, J. A.; Farha, O. K.; Hupp, J. T.; Martinson, A. B. F. Sinter-Resistant Platinum Catalyst Supported by Metal-Organic Framework, *Angew Chem Int Edit* **2018,** *57*, 909-913.

(45) Ikuno, T.; Zheng, J.; Vjunov, A.; Sanchez-Sanchez, M.; Ortuno, M. A.; Pahls, D. R.; Fulton, J. L.; Camaioni, D. M.; Li, Z. Y.; Ray, D.; Mehdi, B. L.; Browning, N. D.; Farha, O. K.; Hupp, J. T.; Cramer, C. J.; Gagliardi, L.; Lercher, J. A. Methane Oxidation to Methanol Catalyzed by Cu-Oxo Clusters Stabilized in NU-1000 Metal-Organic Framework, *J Am Chem Soc* **2017,** *139*, 10294-10301.

(46) Mondloch, J. E.; Katz, M. J.; Planas, N.; Semrouni, D.; Gagliardi, L.; Hupp, J. T.; Farha, O. K. Are Zr-6-based MOFs water stable? Linker hydrolysis vs. capillary-force-driven channel collapse, *Chem Commun* **2014,** *50*, 8944-8946.

(47) Groothaert, M. H.; van Bokhoven, J. A.; Battiston, A. A.; Weckhuysen, B. M.; Schoonheydt, R. A. Bis(mu-oxo)dicopper in Cu-ZSM-5 and its role in the decomposition of NO: A combined in situ XAFS, UV-Vis-Near-IR, and kinetic study, *J Am Chem Soc* **2003,** *125*, 7629-7640.

(48) Giordanino, F.; Borfecchia, E.; Lomachenko, K. A.; Lazzarini, A.; Agostini, G.; Gallo, E.; Soldatov, A. V.; Beato, P.; Bordiga, S.; Lamberti, C. Interaction of NH3 with Cu-SSZ-13 Catalyst: A Complementary FTIR, XANES, and XES Study, *J Phys Chem Lett* **2014,** *5*, 1552-1559.

(49) Oswald, H. R.; Reller, A.; Schmalle, H. W.; Dubler, E. Structure of Copper(Ii) Hydroxide, Cu(Oh)2, *Acta Crystallogr C* **1990,** *46*, 2279-2284.

(50) Frank, P.; Benfatto, M.; Qayyam, M.; Hedman, B.; Hodgson, K. O. A high-resolution XAS study of aqueous Cu(II) in liquid and frozen solutions: Pyramidal, polymorphic, and non-centrosymmetric, *J Chem Phys* **2015,** *142*, 084310.

(51) Fulton, J. L.; Hoffmann, M. M.; Darab, J. G.; Palmer, B. J.; Stern, E. A. Copper(I) and copper(II) coordination structure under hydrothermal conditions at 325 degrees C: An X-ray absorption fine structure and molecular dynamics study, *J Phys Chem A* **2000,** *104*, 11651-11663.

(52) Kirfel, A.; Eichhorn, K. Accurate Structure-Analysis with Synchrotron Radiation - the Electron-Density in Al2o3 and Cu2o, *Acta Crystallogr A* **1990,** *46*, 271-284.

(53) Sheppard, T.; Hamill, C. D.; Goguet, A.; Rooney, D. W.; Thompson, J. M. A low temperature, isothermal gas-phase system for conversion of methane to methanol over Cu-ZSM-5, *Chem Commun* **2014,** *50*, 11053-11055.

(54) Chun, J. W.; Anthony, R. G. Partial Oxidation of Methane, Methanol, and Mixtures of Methane and Methanol, Methane and Ethane, and Methane, Carbon-Dioxide, and Carbon-Monoxide, *Ind Eng Chem Res* **1993,** *32*, 788-795.

(55) Liu, Q. H.; Rogut, J.; Chen, B. S.; Falconer, J. L.; Noble, R. D. Improved methanol yield from methane oxidation in a non-isothermal reactor, *Fuel* **1996,** *75*, 1748-1754.

(56) Takemoto, T.; Tabata, K.; Teng, Y. H.; Nakayama, A.; Suzuki, E. The effects of reaction pressures on the production of methanol through the selective oxidation of methane in CH4-O-2-NOx (x=1 or 2), *Appl Catal a-Gen* **2001,** *205*, 51-59.

(57) Kwak, J. H.; Varga, T.; Peden, C. H. F.; Gao, F.; Hanson, J. C.; Szanyi, J. Following the movement of Cu ions in a SSZ-13 zeolite during dehydration, reduction and adsorption: A combined in situ TP-XRD, XANES/DRIFTS study, *J. Catal.* **2014,** *314*, 83-93.

(58) Alayon, E. M.; Nachtegaal, M.; Ranocchiari, M.; van Bokhoven, J. A. Catalytic conversion of methane to methanol over Cu-mordenite, *Chem Commun* **2012,** *48*, 404-406.

(59) Deka, U.; Juhin, A.; Eilertsen, E. A.; Emerich, H.; Green, M. A.; Korhonen, S. T.; Weckhuysen, B. M.; Beale, A. M. Confirmation of Isolated Cu2+ Ions in SSZ-13 Zeolite as Active Sites in NH3-Selective Catalytic Reduction, *J Phys Chem C* **2012,** *116*, 4809-4818.

(60) Vennestrom, P. N. R.; Janssens, T. V. W.; Kustov, A.; Grill, M.; Puig-Molina, A.; Lundegaard, L. F.; Tiruvalam, R. R.; Concepcion, P.; Corma, A. Influence of lattice stability on hydrothermal deactivation of Cu-ZSM-5 and Cu-IM-5 zeolites for selective catalytic reduction of NOx by NH3, *J Catal* **2014,** *309*, 477-490.

(61) Zhao, Y.; Truhlar, D. G. A new local density functional for main-group thermochemistry, transition metal bonding, thermochemical kinetics, and noncovalent interactions, *J. Chem. Phys.* **2006,** *125*, 194101.

(62) Yang, B.; Gagliardi, L.; Truhlar, D. G. Transition states of spin-forbidden reactions, *Phys. Chem. Chem. Phys.* **2018,** *20*, 4129-4136.

(63) Schroder, D.; Shaik, S.; Schwarz, H. Two-state reactivity as a new concept in organometallic chemistry, *Acc. Chem. Res.* **2000,** *33*, 139-145.

(64) Doan, H. A.; Li, Z. Y.; Farha, O. K.; Hupp, J. T.; Snurr, R. Q. Theoretical insights into direct methane to methanol conversion

over supported dicopper oxo nanoclusters, *Catal Today* **2018,** *312*, 2-9.

(65) Mahyuddin, M. H.; Staykov, A.; Shiota, Y.; Miyanishi, M.; Yoshizawa, K. Roles of Zeolite Confinement and Cu-O-Cu Angle on the Direct Conversion of Methane to Methanol by [Cu-2(mu-O)](2+)-Exchanged AEI, CHA, AFX, and MFI Zeolites, *ACS Catalysis* **2017,** *7*, 3741-3751.

(66) Sushkevich, V. L.; Palagin, D.; van Bokhoven, J. A. The Effect of the Active-Site Structure on the Activity of Copper Mordenite in the Aerobic and Anaerobic Conversion of Methane into Methanol, *Angew Chem Int Edit* **2018,** *57*, 8906-8910.

(67) Yassaghi, G.; Andris, E.; Roithova, J. Reactivity of Copper(III)-Oxo Complexes in the Gas Phase, *Chemphyschem* **2017,** *18*, 2217-2224.

(68) Itoh, S. Developing Mononuclear Copper-Active-Oxygen Complexes Relevant to Reactive Intermediates of Biological Oxidation Reactions, *Acc. Chem. Res.* **2015,** *48*, 2066-2074.

(69) Dietl, N.; van der Linde, C.; Schlangen, M.; Beyer, M. K.; Schwarz, H. Diatomic [CuO](+) and Its Role in the Spin-Selective Hydrogen- and Oxygen-Atom Transfers in the Thermal Activation of Methane, *Angew Chem Int Edit* **2011,** *50*, 4966-4969.

(70) Smeets, P. J.; Hadt, R. G.; Woertink, J. S.; Vanelderen, P.; Schoonheydt, R. A.; Sels, B. F.; Solomon, E. I. Oxygen Precursor to the Reactive Intermediate in Methanol Synthesis by Cu-ZSM-5, *J Am Chem Soc* **2010,** *132*, 14736-14738.

(71) Wang, T. C.; Vermeulen, N. A.; Kim, I. S.; Martinson, A. B. F.; Stoddart, J. F.; Hupp, J. T.; Farha, O. K. Scalable synthesis and post-modification of a mesoporous metal-organic framework called NU-1000, *Nat Protoc* **2016,** *11*, 149-162.

(72) Ravel, B.; Newville, M. ATHENA, ARTEMIS, HEPHAESTUS: data analysis for X-ray absorption spectroscopy using IFEFFIT, *J Synchrotron Radiat* **2005,** *12*, 537-541.

(73) Rehr, J. J.; Kas, J. J.; Vila, F. D.; Prange, M. P.; Jorissen, K. Parameter-free calculations of X-ray spectra with FEFF9, *Phys Chem Chem Phys* **2010,** *12*, 5503-5513.

(74) Frisch, M.; Trucks, G.; Schlegel, H. B.; Scuseria, G.; Robb, M.; Cheeseman, J.; Scalmani, G.; Barone, V.; Mennucci, B.; Petersson, G. Gaussian 09, revision a. 02, gaussian, *Inc., Wallingford, CT* **2009**.

(75) Zhao, Y.; Truhlar, D. G. Benchmark data for interactions in zeolite model complexes and their use for assessment and validation of electronic structure methods, *J Phys Chem C* **2008,** *112*, 6860-6868.

TOC